Preparation of NO-Releasing electrospun chitosan nanofibrous scaffolds for osteoconduction

Chun-Yuan Chiu, Lumapat Paul Noel Quirante, Yu-Tung Hsu, Doan Van Hong Thien, Chung-Hsing Li & Ming-Hua Ho

Published online: 04 Dec 2023.

Submit your article to this journal ⌃

Article views: 961

View related articles ⌃

View Crossmark data ⌃

Citing articles: 2 View citing articles ⌃

Taylor & Francis
Taylor & Francis Group

Preparation of NO-Releasing electrospun chitosan nanofibrous scaffolds for osteoconduction

Chun-Yuan Chiu[a,b], Lumapat Paul Noel Quirante[c], Yu-Tung Hsu[d], Doan Van Hong Thien[e], Chung-Hsing Li[a,b] and Ming-Hua Ho[f,g]

aDepartment of Orthodontics and Pediatrics Dentistry, Tri-Service General Hospital, Taipei, Taiwan, R.O.C; bSchool of Dentistry, National Defense Medical Center, Taipei, Taiwan, ROC; cDepartment of Bioengineering and Biomedical Engineering, Université de Liège, Liège, Belgique; dDepartment of Pharmacy, National Taiwan University, Taipei, Taiwan, ROC; eDepartment of Chemical Engineering, Can Tho University, Can Tho, Viet Nam; fDepartment of Chemical Engineering, National Taiwan University of Science and Technology, Taipei, Taiwan, ROC; gR&D Center for Membrane Technology, National Taiwan University of Science and Technology, Taipei, Taiwan, ROC

ABSTRACT

This study focuses on fabricating sodium nitroprusside-releasing chitosan-based (CS/SNP) nanofibers through electrospinning. Based on SEM images and FTIR spectroscopy, the application of one-step photocrosslinking significantly improved the stability of the nanofibers in aqueous environments. SEM images showed that the porous nanofibrous structure was maintained for up to 24 h. Incorporating SNP into the nanofibrous scaffolds demonstrated an enhanced biocompatibility with osteogenic cells. The cell viability increased with rising SNP content. Enhanced cell attachment, spreading, and proliferation were also observed through fluorescence microscope images of CS/SNP nanofibers, followed by the positive regulation of Smad and Runx2 pathway. The crosstalk between CS and NO reduced the possible toxicity and enhanced the osteoinductivity of NO. Furthermore, the nanofibers contributed to escalated osteogenic differentiation and mineralization, as evidenced by heightened expression of osteogenic markers such as alkaline phosphatase (ALP) expression and calcium deposition. Overall, the photo-crosslinked electrospun CS/SNP nanofibers demonstrate substantial potential as scaffolds in the field of bone tissue engineering.

Introduction

Bone trauma, diseases and damages are major problems in ageing societies. Osteoporosis and other bone diseases mainly affecting the elderly, leading to more than 10.4 million fractures worldwide [1]. In Taiwan, 20% of women and 12% of men over the age of 65 years suffer from vertebral fractures [2]. With a rapidly ageing population, debilitating bone diseases and fractures are only going to rise. Thus, effective solutions to preventing and treating bone defects must be sought.

The autologous bone graft is the current golden standard for critical bone defect therapy. However, complications such as donor site morbidity, pain, paraesthesia, prolonged hospitalization, deep infection, haematoma, inflammation, and restricted availability hound this treatment [3]. New bone therapy strategies have thus been widely studied and developed. Revolutionary methods typically involve transplantation of stem cells, transduction of genes encoding for osteogenic factors, promotion of inherent regeneration capacity of bone via cell-supporting scaffolds, and delivery of osteoinductive biomolecules and substances [4].

Osteoinductive substances often utilized in bone tissue engineering include bone morphogenetic proteins (BMPs) [5–9], peptides [10], naringin [11], and dexamethasone [12]. BMP-2 and BMP-7 are particularly popular and effective, but are very labile and expensive. Therefore, cheaper and more stable alternative substances are worth considering. A possible and interesting candidate is nitric oxide (NO).

NO, a short-lived free radical, is an important signalling molecule in bone. Synthesized from L-arginine by NO synthase (NOS) enzymes, it has been implicated in osteoprogenitor cell differentiation, bone formation and resorption inhibition [13–15]. It is critical for fracture healing with its suppression impairing healing [16]. Due to its nature, NO is difficult to handle with the use of NO donors being widely applied. A commonly studied NO donor is sodium nitroprusside (SNP). SNP is a potent intravenous hypotensive drug used to lower blood pressure during hypotensive and cardiac emergencies, effects attributed mainly to its role as NO donor [17–19]. Systemic supplementation of SNP has been

CONTACT Ming-Hua Ho mhho@mail.ntust.edu.tw Department of Orthodontics and Pediatrics Dentistry, Tri-Service General Hospital, Taipei, Taiwan ROC; Chung-Hsing Li pedoortholi@gmail.com Department of Chemical Engineering, National Taiwan University of Science and Technology, Taipei, Taiwan, ROC

shown to improve fracture healing [16]. Coupled with its stability and availability, SNP was selected as NO donor for this study.

However, NO's effects are biphasic and governed by NO concentration, target cell or tissue, and release profile. At low concentration, it promotes osteoblast proliferation. At high concentration, it inhibits proliferation [13]. The toxicity of NO has been attributed to nitrosative stress from build-up of reactive nitrogen species [20], and activation of apoptotic pathways [21]. SNP is also toxic due to cyanide release [22]. Due to the toxicity, short half-life and multiple therapeutic targets of NO, controlled and localized NO delivery is important to maintain therapeutic effect on defect sites throughout the recovery period while minimizing side effects.

Many NO delivery platforms have been designed and variously applied to prevent infection [23–27] and platelet adhesion [28], promote wound healing [29] and implant integration [30,31] and maintain viability of donated organs [32]. However, there has only been limited work on NO-releasing biomaterials intended for bone repair [16,33]. However, these studies did not thoroughly elaborate on biomaterial design, properties, biocompatibility and osteoinductivity. Thus, this research intends to fill the knowledge gap regarding NO-releasing scaffolds designed for bone tissue engineering.

The nanofibrous membrane is a promising type of delivery drug. Their high surface-to-volume ratio, interconnected three-dimensional porosity, large void volumes to aid cell seeding and penetration, surface microstructure, mechanical strength comparable to physiological stresses, and various controllable features such as degradation and incorporation of growth factors and other bioactive substances have made them particularly attractive for biomedical applications [34,35]. Several methods for nanofiber fabrication exist. Electrospinning is among the most often used for its simplicity, convenience, continuous operation, reproducibility and high encapsulation efficiency which is critical for economic drug delivery. During electrospinning, a polymer jet is ejected from a capillary under the action of an electrical field, stretched and elongated by bending instabilities forming fine fibres, and collected on a grounded collector. Continuous fibres in the nano- to microscales can be easily prepared in this fashion.

Chitosan (CS), a polysaccharide, is a random copolymer of 1,4-D-glucosamine and N-acetyl glucosamine [36,37] usually obtained by alkaline or enzymatic treatment of chitin, the second most abundant natural polymer after cellulose. CS has been considered as a good candidate for drug delivery and tissue engineering applications due to its biocompatibility, biodegradability, low toxicity, mucoadhesivity [38–40] and low immunogenicity [39]. CS-based biomaterials have been widely and successfully applied to bone tissue engineering. As such, CS was selected as the polymer for electrospinning. Our group previously showed that electrospun CS nanofibrous scaffolds are more biocompatible and osteoinductive than dense CS films [41]. Thus, this work envisions a nanofibrous CS scaffold that serves as a tissue engineering scaffold and NO-release platform. The other advantage of CS nanofibers is that the CS can balance the crosstalk between NO and reactive oxygen species (ROS). That is, CS would lead to the depolarization of the mitochondrial membrane, altering the expression of apoptosis caused by NO [42]. Due to the cationic property of CS, the reactive ROS-sensitive linker was suppressed by mitochondria-targeted antioxidants [43]. The biocompatibility of SNP was thus further improved. In this study, we further investigated the mechanism of osteogenic differentiation induced by CS-SNP nanofibers, after the parameters of CS/SNP electrospinning were optimized.

Materials and methods

Materials

Sodium nitroprusside dihydrate (SNP, 99%), chitosan (low molecular weight with a degree of deacetylation 75–85%), trifluoroacetic acid (TFA, 99%), dicloromethane (DCM, 99.8%), acetic acid (99.8%), tetraethylene glycol diacrylate (TTEGDA), 2,2-dimethoxy-2-phenylacetophenone (DMPA, 99%) and sodium carbonate (99.8%) were purchased from Sigma-Aldrich (St. Louis, MO). Calcium hydroxide (95%) was purchased from J.T. Baker (Japan). Sodium hydroxide pellet was obtained from UniRegion Bio-Tech (Taiwan). Potassium bromide was obtained from Fluka (St. Louis, MO, U.S.A.).

For cell culture and *in vitro* analysis, Dulbecco's modified eagle medium (DMEM), foetal bovine serum (FBS), penicillin, trypsin-EDTA were purchased from Gibco Life Technologies (Thermo Fisher Scientific-TW). Kaighn's modification of Ham's F-12 medium was purchased from Manassas (VA, U.S.A.). MTT kit was purchased from Carlsbad (CA, U.S.A.) Dimethyl sulphoxide (99.9%) was purchased from J.T. Baker (Japan). Zinc chloride (98%), calcium chloride (99%), glycine (99%), 4-nitrophenyl phosphate disodium salt hexahydrate (p-NPP), CellLytic™ M cell lysis reagent, 25% glutaradehyde in PBS, dexamethasone (97%), L-ascorbic acid (98%), β-glycerophosphate disodium hydrate (99%), phalloidin-Atto488, 4',6-Diamidino-2-phenylindole dihydrochloride (DAPI, 98%), triton X-100, bovine serum albumin (BSA, 98%), CF594-conjugated goat anti-mouse IgG, mouse monoclonal anti-vinculin IgG, goat polyclonal anti-human osteopontin IgG, CF647-conjugated rabbit anti-goat IgG, Griess reagent

(modified), sodium nitrite (99%) and hydrochloric acid (37%) were purchased from Sigma-Aldrich (St. Louis, MO). Micro BCA™ protein assay kit was obtained from ThermoScientific (IL, U.S.A.). Formaldehyde in aqueous PBS (10% v/v) was obtained Mallinckrodt Baker (KY, U.S.A.). Ethylenediaminetetraacetic acid (EDTA) disodium salt was purchased from Kanto Chemical Co, Inc (Tokyo, Japan). Sodium sulphide nonahydrate (98%) was purchased from Acros Organics (NJ, U.S.A.). Hydrazine sulphate was purchased from J.T. Baker Company (Japan). Distilled deionized (DI) water was used throughout the experiment.

Preparation of chitosan nanofibers

CS (low molecular weight) solutions with concentrations of 80 mg/mL were prepared by dissolving pre-weighed CS powder into two-solvent system of trifluoroacetic acid (TFA) and dichloromethane (DCM) mixed at volume ratio of 7:3. For SNP-containing scaffolds, SNP was added by mixing into CS solution. The solution was stirred at speed of 500 rpm and temperature of 32°C for 24 h. Five to six hours prior to electrospinning, tetraethylene glycol diacrylate (TTEGDA) photo-crosslinker and 2,2-dimethoxy-2-phenylacetophenone (DMPA) were added into the CS/SNP solution. The solution was then stirred for 5–6 h until homogeneous.

A syringe (3 mL) was filled with prepared CS/SNP solution and placed in electrospinning syringe pump and connected to a high voltage power supply. A grounded aluminium collector and $1 \times 1 \, cm^2$ cover glass slips were set 12 cm below syringe needle. Then, polymer solution was pumped out at flow rate of 0.2 mL/h under a voltage difference of 17 kV. Electrospinning was carried out at 26–29°C for 3 or 5 h. UV lamps were turned on through electrospinning duration for photo-crosslinked samples. Then, CS/SNP nanofibers were dried in ambient temperatures overnight before further characterization. Chamber humidity was maintained around 40–60%.

In this study, TTEGDA concentration was varied from 0 to 10 wt% while DMPA concentration is held constant at 1.5 w.%. Weight percentages are based on the total CS amount. UV power is varied from 0 to 160 W.

Neutralization of CS/SNP nanofibers was carried out by immersing membranes in a strongly alkaline solution. Nanofibers were treated with 5 M aqueous sodium carbonate solution for 1 h at 50°C. After immersion, membranes were repeatedly washed with DI water for 5 min each until neutral. Membranes were then dehydrated in 70% ethanol for 10 min. After carefully removing superficial liquid using filter paper, membranes were dried at ambient conditions for 1 day. Samples were further oven-dried at 40°C overnight prior to further characterization and experimentation.

FE-SEM (field emission scanning electron microscope) analysis

SEM (JEOL JSM-6390LV, Japan) images were taken to analyse the morphology of nanofibers. Membrane samples were stuck onto sample platform using copper tapes and coated with platinum using a JEOL JFC-1100 E sputtering device for 90 s. Platinum-coated samples were loaded into a JSM-6390LV scanning electron microscope (JEOL, Japan). Nanofibers were observed at an acceleration voltage of 15–20 kV. Selected SEM images were used to observe nanofiber morphology and structure after electrospinning. Specifically, these images were used for determining nanofiber diameter and diameter distribution using ImageJ software. Average nanofiber diameter was calculated from at least forty fibres per sample.

Fourier Transform Infrared (FTIR) spectroscopy

FTIR spectra of membranes were collected using a FTS-3500 Excalibur FTIR spectrometer (Varian Inc.) equipped with KBr beam splitter. The spectra were recorded at resolution of 4000–$400 \, cm^{-1}$ in absorbance mode.

For unneutralized CS/SNP nanofibers, an attenuated total reflection (ATR) add-on was utilized. Samples IR spectra were obtained as-spun on aluminium collectors. Blank aluminium foil was used as background.

For neutralized CS/SNP nanofibers, membrane samples were scraped off glass slide collectors and ground using mortar and pestle. Resulting powder was mixed with KBr powder and compressed into disks. Samples were loaded into FTIR spectrometer without ATR attachment. Pure KBr spectra was used as background.

Swelling test

Hydrophilic CS nanofibers easily take up water in aqueous environments causing swelling and loss of nanofibrous structure, necessitating photo-crosslinking of nanofibers to improve their mechanical properties. To evaluate the effectivity of photo-crosslinking on nanofibers' mechanical performance, electrospun CS/SNP nanofibers photo-crosslinked at different conditions were immersed in PBS for 24 h. After immersion, samples were gently blotted with filter paper to remove superficial moisture. Samples were then dried at room temperature for at least 1 day and were then analysed using SEM to evaluate surface morphology after immersion.

SNP and NO assay

Quantification of SNP for *in vitro* drug release was performed using the method described by Vesey and Batistoni [44]. The assay is based on the colour reaction of SNP and sulphides in basic pH which produces an intense red-purple colour with maximum absorbance at 540 nm.

Nanofibrous samples were immersed in 1× PBS with aliquots being drawn at certain time points. Samples were mixed with 0.1 M EDTA solution and colour development reagent at a volume ratio of 1:1.5:1. Colour was allowed to develop for 10 min before absorbance at 540 nm was measured using MQX200R microplate reader (Bio-Tek Instrument Inc., U.S.A.). Entire assay was performed in the dark. A calibration curve was constructed using SNP standard. Colour development reagent comprised 5 g sodium sulphide, 50 mg hydrazine sulphate and 20 g sodium hydroxide dissolved in 1 L DI water which was freshly prepared every 3 days.

The amount of NO was captured using the Apollo 1000 free radical analyser and MOPF100 NO microsensor. The radical concentrations were recorded and analysed before the microsensors were polarized by 0.1 M $CuSO_4$ solution under continuous stirring. During polarization, the background sensor current, observed as the baseline on a current-time chart, decreased slowly.

Cell culture

Nanofibrous membranes with $1\,cm^2$ were sterilized and placed in 24-well plates. 7F2 cells were seeded on each membrane at an initial density of 5000 cells/mL. Cell-seeded scaffolds were maintained in an incubator at 37°C with 5% CO_2. Culture medium was renewed every 2 days. On selected time points, cells were harvested, and prepared for observation either via SEM or fluorescence microscopy.

Harvested cells were washed in PBS, initially fixed with 0.2% GA for 10 min, and further fixed with 2.5% GA for 2 h. After repeated washing with PBS, samples were serially dehydrated in graded ethanol solutions, in order: 30%, 50%, 70%, 80%, 90%, 95%, and 99.9% ethanol for 10 min each. Dehydration in absolute ethanol was repeated 3 times. Samples were dried in a Samdri-PVT-3D critical point dryer (Tousimis, Inc., U.S.A.). Cells were observed by SEM.

Analysis of Runx and smad expression and immunocytochemical staining

To measure the levels of *Runx1* and *Runx2* mRNA in mouse granulosa cells, primers for mouse *Runx1* and *Runx2* were designed using the Primer Express 2.0 software, whereas the GAPDH primers and probe

were purchased from Applied Biosystems (Foster City, CA). Real-time PCR was performed using either SYBR Green (*Runx1* and *Runx2*) or TaqMan (*GAPDH*) [45].

For Smad1 and Smad6 analysis, protein extractions of lysed cells were fractionated by 10% SDS-PAGE, electroblotted onto a Hybond-P membrane, which was probed with antibodies to Smad1 and P-Smad1, or with antibodies to Smad6 and P-Smad6. Then, samples were developed using an ECF Western blotting kit (Amersham Pharmacia Biotech) and visualized using a Typhoon 9410 Imager (Amersham Biosciences, Piscataway, NJ).

Harvested cells were washed in PBS for 5 min, and quickly fixed in 3.7% formaldehyde for 10 min. After repeated washing with PBS, samples were treated with 0.1% Triton X-100 for 5 min. Cells were washed twice to remove remaining surfactant. To block non-specific interactions, samples were immersed in 1% BSA solution for 10 min. After removing solution, samples were incubated in primary antibody diluted in blocking medium for 1 h at room temperature or overnight at 4°C. After rinsing with 1× PBS, samples were incubated in secondary antibody and phalloidin-Atto 488 (1:4000 in PBS) at room temperature for 1 hour. Nuclei were counterstained with DAPI (1:1000) for 30 min. Cells were observed under fluorescence microscope.

For cytoskeleton staining, primary antibody was mouse anti-vinculin monoclonal IgG (1:800) that was labelled with CF594-conjugated goat anti-mouse IgG. For osteopontin labelling, primary antibody was goat anti-human osteopontin polyclonal IgG (1:100) that was labelled with CF647-conjugated rabbit anti-goat IgG.

Cell viability tests

To evaluate cell viability via MTT reduction, cultured cells were harvested on selected time points, rinsed with PBS, and transferred into new 24-well plates. Each well was added with 400 µL MTT working solution. After incubating for 4 h, working solutions were carefully withdrawn, and replaced with 600 µL DMSO. After shaking for 15 min, 200 µL aliquots were taken and placed in 96-well plates. Absorbance at 570 nm of samples were measured using MQX200R microplate reader (Bio-Tek Instrument Inc., U.S.A.. Entire assay was performed in the dark.

To prepare MTT working solution, MTT powder was placed in light-protected tube, and dissolved in PBS to prepare 5 mg/mL MTT stock solution. In laminar hood, stock solution was filtered through 0.22 µm membrane filter and diluted with PBS to ratio of 1:9 (v/v). Solution was repeatedly aspirated and dispensed to completely mix.

ALPase expression

ALPase is an early marker for cell differentiation towards the osteocytic phenotype. The hydrolysis of p-nitrophenyl phosphate (p-NPP) by action of ALPase results in p-nitrophenol, which has a strong absorbance at 405 nm, is the basis for ALPase activity quantification. Murine 7F2 osteoblast cells were seeded on scaffolds in 24-well plates at a density of 5000 cells/mL and incubated at 37°C with 5% CO_2. At each time point, scaffolds were washed twice with PBS, and lysed with 0.2 mL lysis buffer for 15 min. Lysate was treated with 0.600 mL ALPase buffer for 30 min. Reaction was stopped by treating with 0.15 mL 3N NaOH at 4°C for 10 min. Then, absorbance was read at 405 nm using MQX200R microplate reader.

ALPase buffer was prepared by dissolving $MgCl_2$ (1 mM), $ZnCl_2$ (1 mM), and glycine (0.1 M) in deionized water. After adjusting to pH 10.4, p-NPP tablets were dissolved to prepare 1 mg/mL solution.

ALP activity was normalized to total protein to correct for differences in cell number. Total protein was measured via bicinchoninic acid (BCA) assay. A modification on the biuret reaction of Cu(II) ions with proteins, the BCA assay has better sensitivity due to the intense colour of Cu(I) ions with bicinchoninic acid.

For this assay, lysate from 7F2 cells cultured on CS/SNP nanofibers and BCA working reagent were mixed and placed in 96-well plates. Mixtures were incubated at 37°C for 2 h. After, incubation, absorbance was quantified at 562 nm using a microplate reader.

Statistical analysis

All data were presented as mean ± standard deviation. Statistical significance between the two specified groups was assessed using a two-tailed Student's t-test. For groups containing more than two datasets, a one-way ANOVA was employed. Each treatment consistently included more than four replicates. A p-value less than 0.1, 0.05, or 0.01 was considered statistically significant. The statistical calculations were conducted using MINITAB software.

Results and discussion

Morphologies and composition of CS/SNP nanofibers

CS solutions with SNP contents of 0–50% were electrospun and SEM images are shown in Figure 1. The electrospinnability of CS/SNP solutions was dependent on SNP content. At SNP loadings with 0 to 20%, nanofibers were uniform, fine, continuous, and randomly oriented in Figure 1(a). No significant beads-in-string morphologies were observed, though the fibre diameters were much varied at SNP concentration of 20%. When SNP content was raised to 30%, spindle-shaped irregularities were seen. Further increase in SNP loading to 40% led to the formation of spherical beads along the nanofiber length. At SNP loading of 50% and above, nanofibers were no longer formed. Using ImageJ software, the diameters of nanofibers (0–30% SNP) were measured. From Figure 1(b), the average nanofiber diameter was unaffected by SNP content, but the diameter variation increased with SNP addition.

The CS/SNP solutions containing less than 30% SNP were able to form uniform and homogenous nanofibers, and the optimized conditions were similar to the electrospinning of pure CS [37]. However, previous research indicated that adding salts to polymer solutions would affect solution electrical conductivity [46,47] and viscosity [48], two critical factors for electrospinning. These two parameters may promote bead formation by raising jet instability [49,50], which would be the reason for the difficulty in obtaining homogenous nanofibers. In previous studies, it was common to blend other polymers to enhance electrospinnability when using additives [11,23,37]. However, in this research, pure CS combined with SNP demonstrated excellent spinnability. Moreover, our study suggested that the properties of the CS solution remained largely unaltered with SNP concentrations below 30%. This research clearly established the remarkable electrospinnability of SNP in the CS solution.

The IR spectra of pure (CS NF) and SNP-loaded (SNP 10% CS NF) nanofibers are presented in Figure 1 (c). The characteristic peaks of CS nanofibers in IR spectra showed a strong absorbance from protonated N-H at 1675 cm^{-1}, N-H stretching band at 1580 cm^{-1}, CH_2 bending at 1407 cm^{-1}, CH_3 symmetrical deformation at 1348 cm^{-1}, CH vibration band at 1153 cm^{-1}, and a broad peak at 1030–1081 cm^{-1} for CO stretching vibration [51]. From the IR spectra, indications of the presence of SNP were seen at 1940 cm^{-1}, which is correspondent to the NO moiety in SNP in previous research [52].

To improve the stability of nanofibers in an aqueous environment for cell culture or following biomedical applications, the CS and CS-SNP nanofibers were treated by photo-crosslinker, TTEGDA, and photo-initiator, DMPA, under UV irradiation in the electrospinning process. DMPA decomposed under UV exposure. Then, the methylated DMPA segment activated the acrylate double bond of TTEGDA to initiate the photo-crosslinking reaction. The propagation of TTEGDA monomers eventually formed a network with CS nanofibers [53]. The SEM images of photocrosslinked fibres are presented in Figure 2(a), indicating the unchanged nano-structures after crosslinking. The fibre diameters from SEM images were calculated and
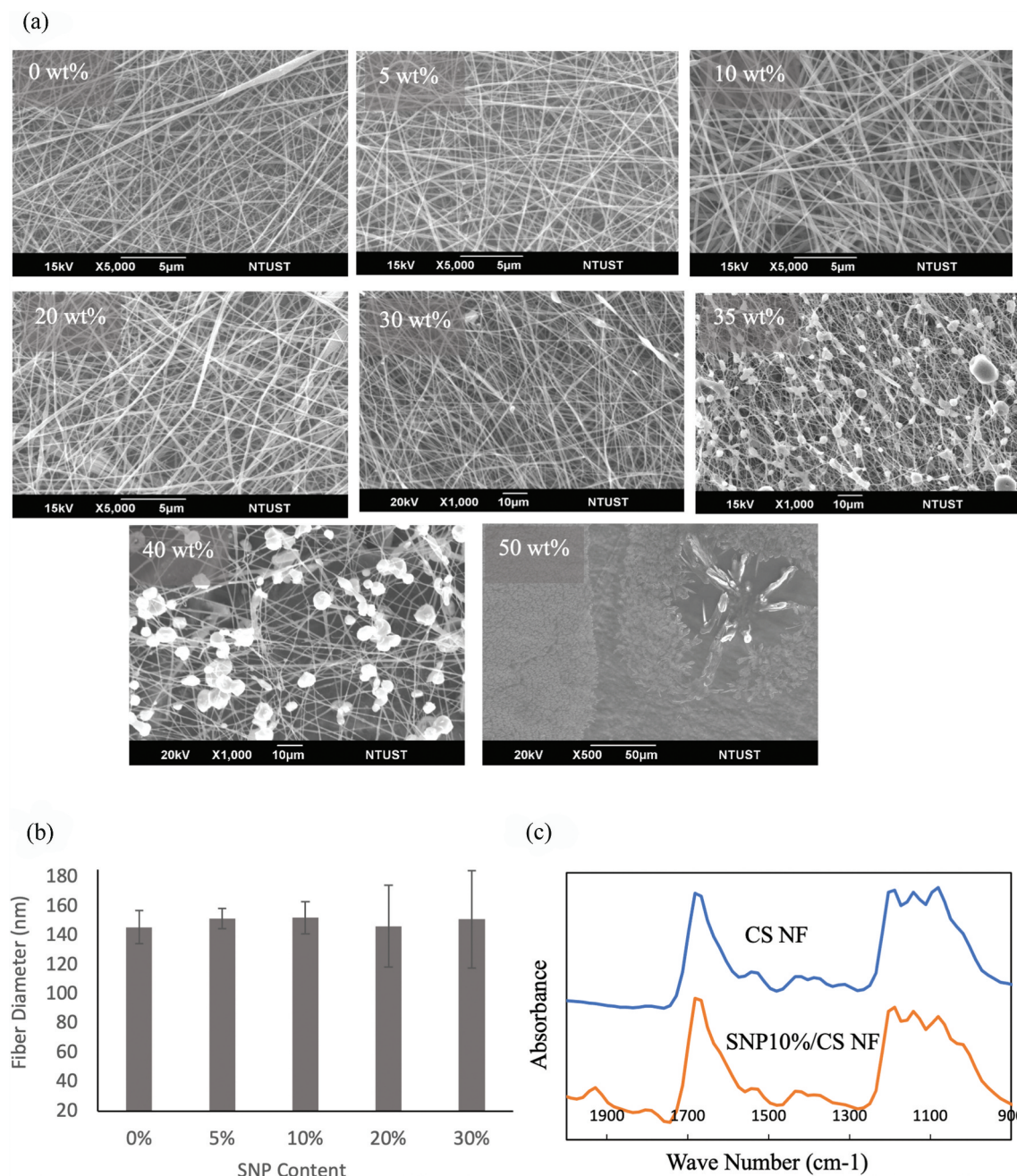
(a)

(b)

(c)

Figure 1. Characterization of CS/SNP nanofibers with various SNP loading. (a) SEM images of electrospun CS/SNP nanofibers. (b) diameters of CS/NP nanofibers evaluated according to SEM images. (c) IR spectra of CS and CS/SNP nanofibers. All the given percentages are mass percentages with respect to the CS amount.

presented in Figure 2 (b), proving that the fibre diameter was not significantly changed due to TTEGDA crosslinking.

UV energy used for irradiation was investigated with 5 wt% TTEGDA and 1.5 wt% DMPA. SEM images in Figure 2(c) show that CS/SNP nanofibers were generally continuous, uniform, and smooth when UV irradiation ranged from 0 to 160W. Image analysis of photo-crosslinked CS/SNP nanofibers in Figure 2(d) reveals the unchanged fibre diameter treated with different UV irradiation energies. This may be due to entanglement relaxation brought by SNP addition counteracting the reported increase in viscosity by high-power

irradiation [46]. Thus, the UV irradiation did not drastically change the electrospinnability of CS/SNP solutions, meaning that the stability of the Taylor cone in the spinning process was not influenced but enhanced.

Figure 3(a) shows the nanofiber morphologies immersed in PBS aqueous solution after 24 hours, where the nanofibers were crosslinked with 0, 2.5, 5 and 10% TTEGDA, respectively. The CS/SNP nanofibers without TTEGDA crosslinking (0 wt%) were highly swelled after a 24-hour immersion, where the nanofibrous structures were almost destroyed completely. On the contrary, with photo-crosslinking, the nanofibrous structures could be maintained in PBS.
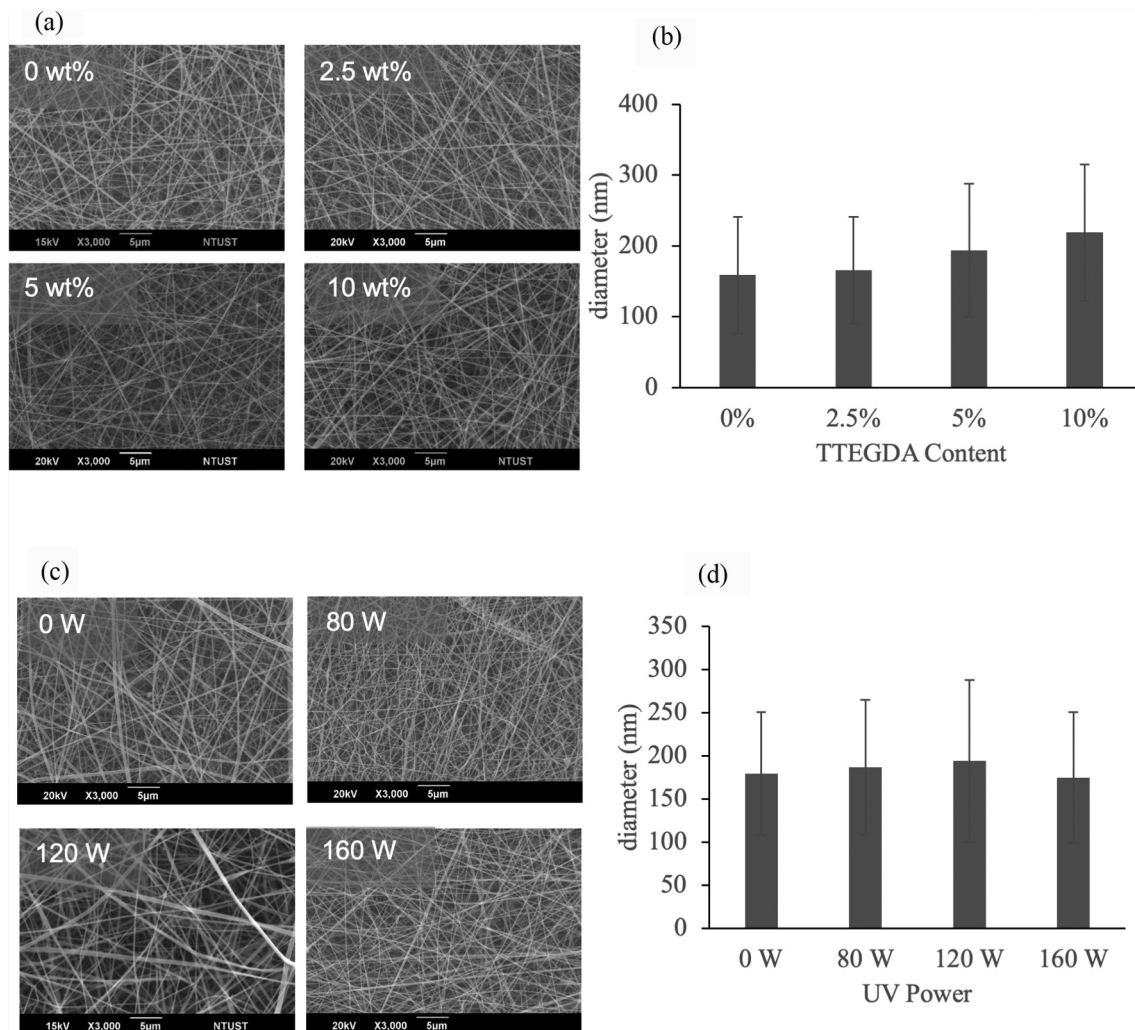
Figure 2. Morphologies of photo-crosslinked CS/SNP nanofibers. (a) SEM images of CS/10% SNP nanofibers with 0, 2.5, 5 and 10% TTEGDA. (b) diameters of CS/10% SNP nanofibers with 0, 2.5, 5 and 10% TTEGDA. (c) SEM images of photo-crosslinked electrospun CS/10% SNP nanofibers exposed to 0, 80, 120, 160 W UV irradiation in the spinning process. (d) diameters of photo-crosslinked electrospun CS/10% SNP nanofibers exposed to 0, 80, 120, 160 W UV irradiation in the spinning process. The amount of SNP was fixed as 10 g SNP/100 g CS.

When the TTEGDA concentrations were 5% and 10%, the structures of CS/SNP were roughly unchanged after a one-day immersion. The results indicate that the one-step TTEGDA photo-crosslinking process was seamlessly integrated with the electrospinning method, significantly improving the stability of CS/SNP nanofibers in an aqueous solution. This enhanced nanofiber stability is particularly crucial when incorporating hydrophilic additives like SNP. The photo-crosslinking effectively mitigated burst release, thereby preventing potential side effects.

From Figure 3(b), the delivery profile of SNP from nanofibrous membranes was a typical diffusion-driven release platform. Nanofibers with higher SNP loading were able to release more SNP. However, no matter whether nanofibers contained 10% or 20% SNP, the burst release was effectively hindered by crosslinking. The photocrosslinking enhanced the mass-transfer resistance of CS nanofibers, successfully reducing the sudden release of SNP.

Without photo-crosslinking (CS/10% SNP), the NO release reached 99% just in one day, as revealed in Figure 3(c). Previous studies have reported a high local concentration of NO caused by burst release as cytotoxic [22]. In contrast, the photo-crosslinking process reduced the excessive release of NO from CS nanofibers containing SNP, thereby preventing cytotoxicity induced by elevated local NO concentrations. After 2 days, the released NO content was equivalent to 13.3 μM (24%) which was not cytotoxic and comparable to S-nitrosated PLGH-cysteine nanofibers developed by Wold *et al* [54], suggesting potential improved biocompatibility.

By comparing the results in Figure 3(b and c), the release of NO was modulated by CS nanofibers effectively. After 2 days, photocrosslinked CS/10% SNP released 35% SNP when NO was released by 24%. After a 4-day immersion, SNP was released by 45% when NO was released by 48%. The results supported that the release slope of NO was lower than that of SNP. The reason is possibly because the CS nanofibers played
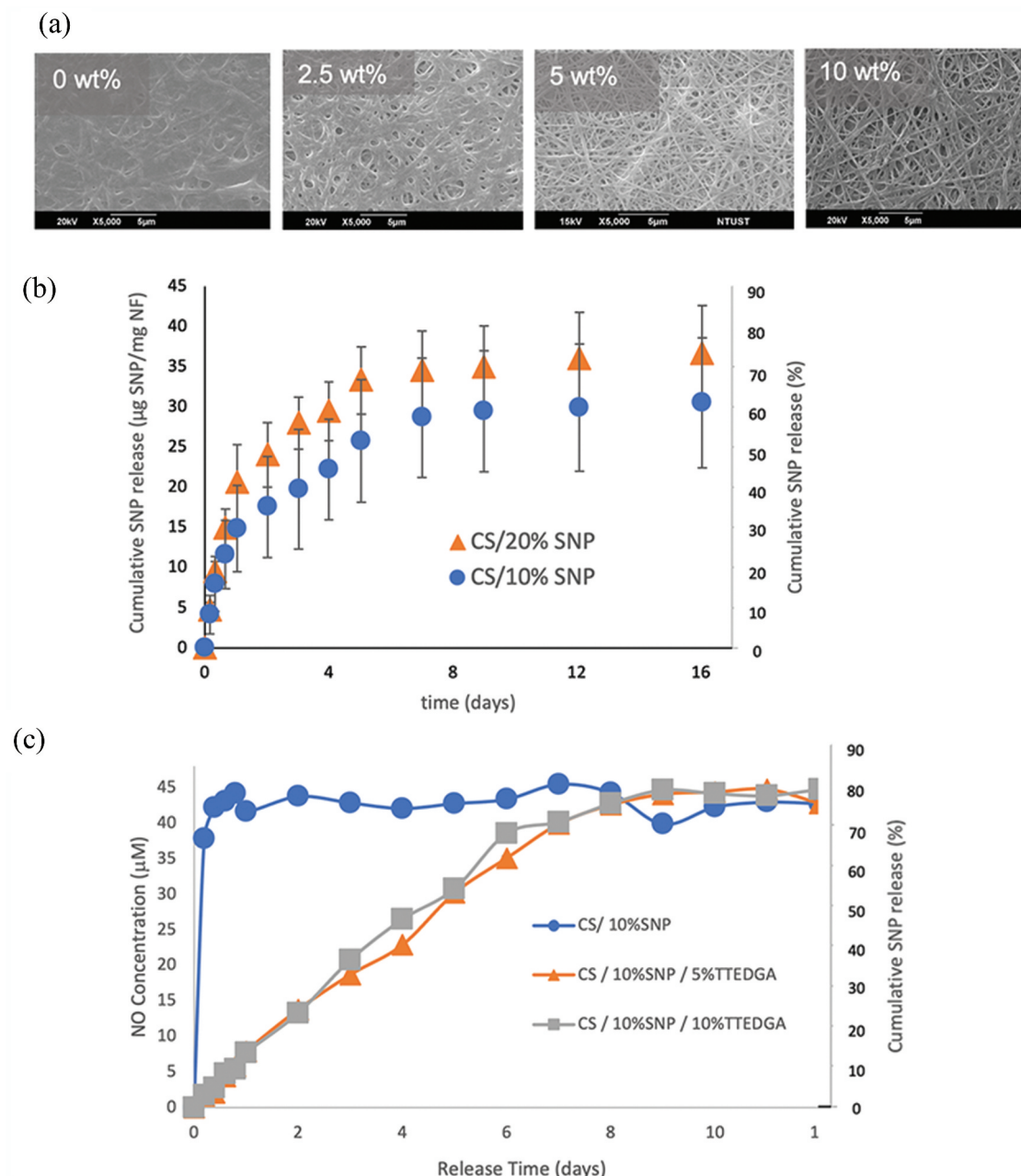
(a)

(b)

(c)

Figure 3. (a) SEM images of photo-crosslinked CS nanofibers with 10% SNP, 5% TTEGDA and irradiation of 120W. (b) SNP release from CS nanofibers with 10% SNP and 20% SNP, which are photocrosslinked by 10% TTEGDA and 120W irradiation. (c) NO release from CS nanofibers containing 10% SNP without photocrosslinking, with 5% TTEGDA photocrosslinking and with 10% TTEGDA photocrosslinking under 120W irradiation.

a role as a reservoir of NO. Thus, the release of NO would be adjusted by the crosstalk between CS and NO, reducing the possible toxicity of NO. The interaction between CS and NO was previously suggested by Lu et al. [23], where the CS matrix was noted for its ability to deliver NO gradually rather than through immediate release. However, it's important to note that this interaction between CS and NO is being reported for the first time in the current study. Figure 3(c) presents that after 9 days, the NO release at a steady-state reached about 90–100%. In previous studies, the majority of NO-releasing devices released their payload within a few hours [55] to one day [54]. The comparatively extended release duration of CS/SNP nanofibers in this study was attributed to the interplay between NO and CS, and this interaction was further enhanced by CS crosslinking. Essentially, the synergy between NO and CS, coupled with the increased stability resulting from photocrosslinking, is expected to further augment the osteoinductive effects of CS/SNP nanofibers.

Cell attachment and morphology on CS/SNP nanofibers

The morphologies of osteoblasts grown on CS/SNP electrospun nanofibers were investigated in Figure 4. From Figure 4(a), there was no clear difference in cell attachment on SNP-free (0 wt%)

and SNP-containing (10 wt%) CS films. That was, the CS films would not present the effects of encapsulated SNP on cell proliferation and attachment. On the contrary, the addition of SNP encouraged the spreading of osteoblasts when CS nanofibers were applied instead of CS films. The cell densities were higher on CS/SNP nanofibers, and distinct and clear lamellipodia formation and filopodia extension were visible in Figs. 4(b).

From CS/10 wt% SNP films in Figure 4(a) and nanofibers in Figure 4(b), more cells growing on nanofibrous scaffolds compared to dense films. However, lamellipodia on CS film were rounder and broader compared to the tighter and more angular morphology observed on cells cultured on nanofibers. Among nanofibrous membranes, SNP content did not significantly affect the number of attached cells, but cell spreading was greater on SNP-rich scaffolds. On CS/20 wt% SNP and CS/30 wt% SNP, some cells occupied very large areas. Cell–cell adherent junctions between these cells were clear (white arrows, 20 wt% and 30 wt% in Figure 4(b). In summary, the cell attachment increased by applying nanofibers instead of films. The SNP contents improved the activation of cytoskeletons, inducing the expression of cell–cell junctions.

On day 3, vinculin expression in Figure 5 was higher in osteoblasts cultured on SNP-loaded nanofibers in comparison to SNP-free nanofibers (0 wt%). The intensity of positive signals of vinculin was significantly higher on CS nanofibers with 20 wt% SNP loading. A long section coinciding with the edges of several cells touching indicated cell–cell junctions.

The strong response of vinculin, a cytoskeletal protein associated with both cell–cell and cell–material interactions [56], is an indicator of excellent cell spreading. Its clear expression in these fluorescence images confirmed the cytoskeleton activation by CS/SNP nanofibers. The cellular adhesion would be highly correlated with differentiation through the cascade pathway; that is, the cell-material binding would initiate signalling cascades regulating cell fate [57,58].

Phosphorylation of Smad1 and Smad6 was examined to further investigate the effects of SNP/NO release. Smad1, one of the receptor Smad proteins, acts in response to BMPs [20], while Smad6 (inhibitory Smad) is structurally divergent from the other Smads and antagonizes signal transduction. The analysis of Smad1 and Smad6 phosphorylation is illustrated in Figure 6. Figure 6 (a) shows that phosphorylation of Smad1 increased by two factors,
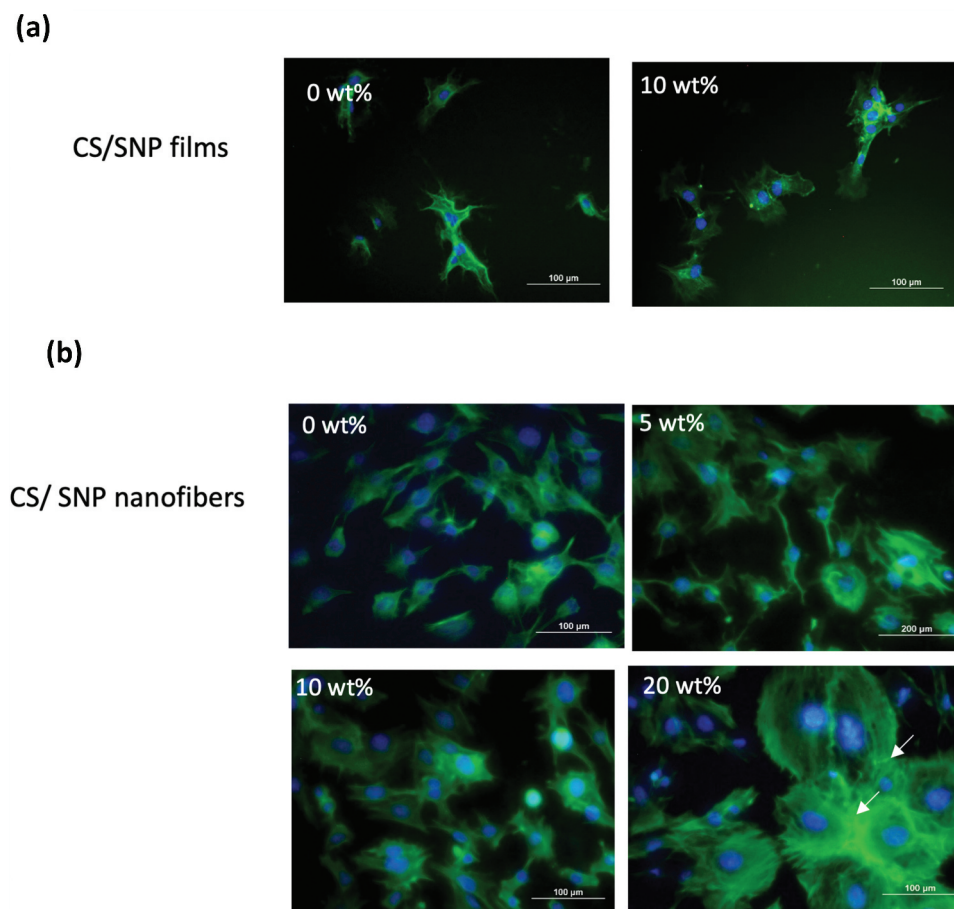
(a)

(b)

Figure 4. Cytoskeleton fluorescence images of osteoblasts cultured for 3 days on CS/SNP films and nanofibers with various SNP contents. F-actin and nucleus are labeled green and blue, respectively. All the CS nanofibers were photocrosslinked with 5% DMPA and with 10% TTEGDA under 120W irradiation. All given percentages are weight percentages with respect to total CS.
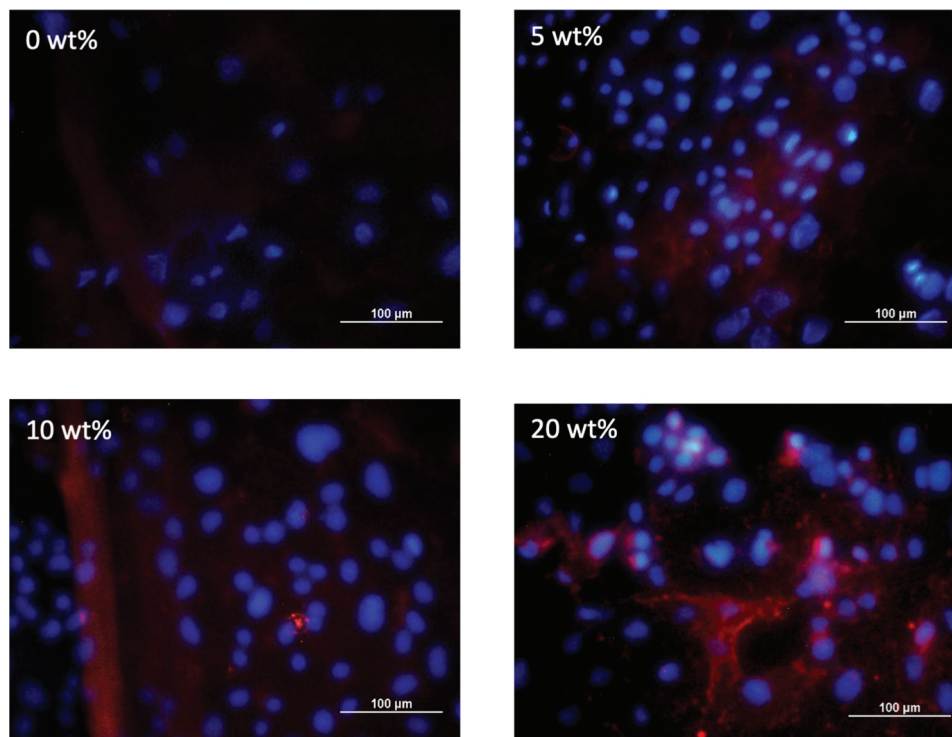
Figure 5. Vinculin expression of 7F2 cells cultured for 5 days on CS/SNP nanofibers containing 0, 5, 10 and 20 wt% SNP. Vinculin and nucleus are labeled as blue and red, respectively.

which were nanofibrous structures and SNP loading. The results indicate that the Smad1 phosphorylation was promoted by 75% when CS nanofibers were applied instead of films ($p < 0.01$), and the P-Smad1/Smad1 ratio was enhanced by 181% as SNP content increased from 0 wt% to 20 wt%. Since Smad1 plays an important role in transducing osteogenic receptor molecules and in mediating biomineralization signalling, the results provide evidence that nanofibers and NO release are highly effective promoters of bone formation due to their enhancement in osteogenic responses.

Figure 6(b) shows the Smad6 phosphorylation of osteoblasts. The results suggest that nanofibers and SNP loading suppressed the expression of Smad6. CS nanofibers decreased Smad6 phosphorylation by about 16%, compared with CS films. The Smad6 suppression was less efficient than the Smad1 promotion due to nanofibrous structures. With SNP loading of 20 wt%, Smad6 expression was inhibited by 71%. Smad6 interferes with phosphorylation of receptor Smads and negatively regulates TGF-β signalling [22]. The suppression of TGF-β signalling would inhibit osteogenic differentiation; in other words, the inhibition of Smad6 would promote osteogenic differentiation. Thus, the results in Figure 6(b) reveal that the enhanced cell spreading caused by nanofibrous structures and SNP delivery would be osteoconductive by inhibiting Smad6 expression. Moreover, the SNP release was more effective than nanofibers, corresponding to the tendency in Smad1 expression.

The Smad1 activation and Smad6 inhibition explain the pathway initiated by cytoskeleton anchoring after accepting released NO and attaching to nanofibers.

From Figure 6(c), the Runx2 expression was enhanced by 37.5% when nanofibers were applied instead of films, and 20% SNP loading increased Runx2 regulation by 645% relative to nanofibers without SNP (0 wt%). That is, the loaded SNP efficiently delivered NO (as Figure 3) to cellular receptors, initiating Smad and Runx2 expressions through cytoskeleton activation [59,60]. Kim et al. [61] claimed that NO would induce BMP expression, where NO itself or cGMP (latter produced by NO signalling) promotes osteoblastic metabolism. In osteogenic cells, Erk-mediated spreading and migration were found to be NO/cGMP/PKG-dependent [62,63], initiating the Smad pathway. These research support our results that after the cytoskeleton activation, Runx2 and Smad expression were promoted, which would enhance osteogenic differentiation.

On the other hand, Figure 6 presents that the Smad1, Smad6 and Runx2 were not significantly regulated by the SNP loading on CS film. According to Figure 4(a), the cytoskeleton was not activated due to SNP addition in CS film. Thus, it is inferred that the cytoskeleton expression was enhanced by nanofibrous structures first, followed by the Smad and Runx2 regulation induced due to NO release. Huang et al. reported that in the BMP pathway, the Runx2 would be negatively regulated or not influenced if Smad was not activated or
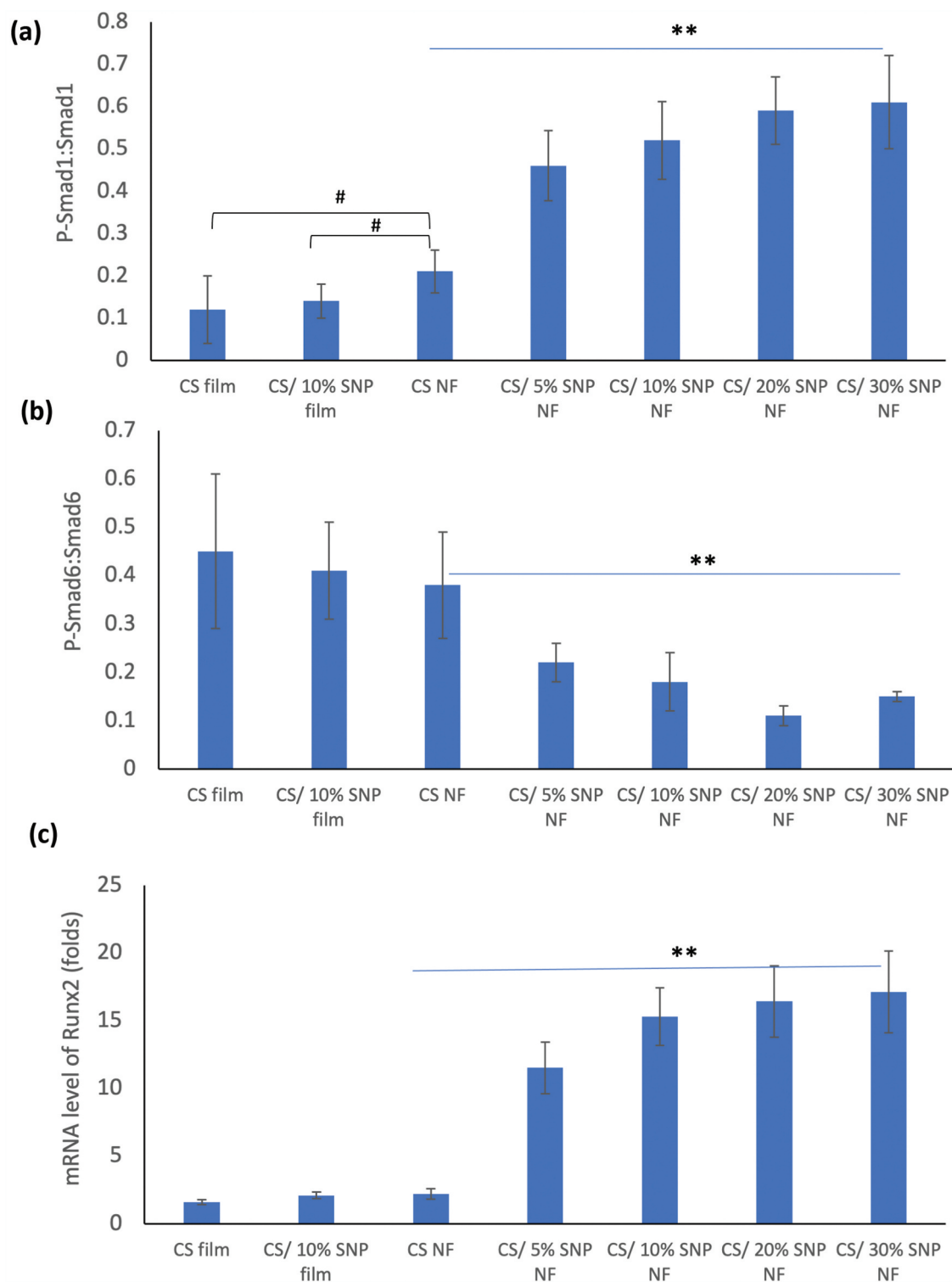
Figure 6. Smad and Runx2 expression of osteoblasts (a) phosphorylation of Smad1 in terms of P-Smad1/Smad1. (b) phosphorylation of Smad6 in terms of P-Smad6/Smad6. (c) the mRNA level of Runx2 relative to GAPDH. The significant differences between two indicated were denoted by #($p < 0.1$) according to a two-tailed t-test ($n > 4$). The significant differences of the groups below the same horizontal line were denoted by **($p < 0.05$) according to ANOVA test ($n > 4$).

inhibited [64], corresponding to our results. Based on the finding from Smad and Runx2 expression, it is inferred that the CS film was not effective on Smad phosphorylation, which was possibly caused by the inactivated cytoskeleton. Thus, Runx2 was not positively regulated on CS film even though SNP was loaded.

After the pathway of mRNA expression was identified, the cell viability and makers of osteogenic differentiation were analysed in the following experiments. From Figure 7(a), the cell viability was clearly promoted by SNP loading in nanofibers and increased with the SNP content. Moreover, the nanofibrous structures enhanced the cell viability. Figures 7(b and c) show
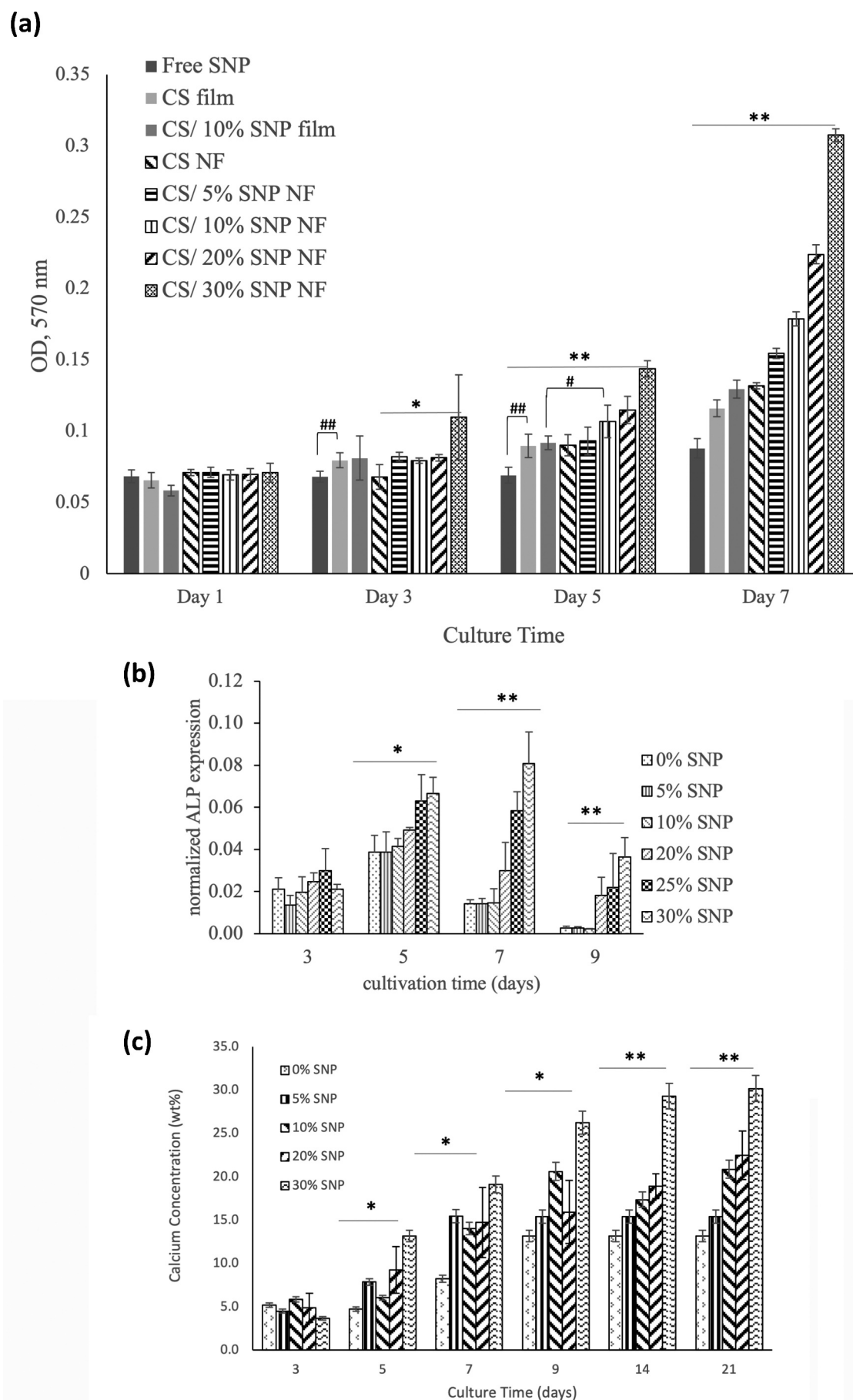
Figure 7. (a) cell viability with free SNP addition and on various CS scaffolds, including CS film, CS NF, CS film with 10% SNP (CS/ 10% SNP film), and CS NF with the addition of 5%, 10%, 20% and 30% SNP. The significant differences between two indicated were denoted by #($p < 0.1$) and ##($p < 0.05$) according to a two-tailed t-test ($n > 4$). The significant differences of the groups below the same horizontal line were denoted by *($p < 0.1$) and **($p < 0.05$) according to ANOVA test ($n > 4$). Figure 7 (b) ALP expression and (c) calcium deposition of 7F2 cells on CS/SNP nanofibers with differing SNP content and spinning time in osteogenic differentiation medium. The significant differences of the groups below the same horizontal line were denoted by *($p < 0.05$) and **($p < 0.01$) according to ANOVA test ($n > 4$).

that the osteogenic differentiation was promoted by SNP loaded in CS nanofibers and increased with the SNP content. The results support that the CS nanofibrous scaffolds containing SNP were highly osteoconductive, which was the downstream differentiation following Smad and Runx2 activation.

Based on mRNA expression and osteogenic markers, the presence of a high SNP content enhanced the activation of Smad1 and Runx2, while it suppressed Smad6 under similar conditions. There was no statistically significant difference between SNP concentrations of 20 wt% and 30 wt%. The regulation of Smad and Runx2 proved to be highly efficient when the SNP concentration exceeded 20 wt%. Furthermore, cell viability, ALP expression, and calcium deposition consistently and gradually increased with higher SNP contents.

Among all the tested scenarios, the nanofibers with the highest SNP concentration of 30 wt% exhibited the most favourable osteoconductive effects in this study. This suggests that these indicators of osteogenic differentiation were highly responsive to the SNP content during the culture process. It's worth noting that the Smad and Runx2 pathways induced by SNP/CS nanofibers were reported for the first time in this research, thereby demonstrating the osteoinductive effects of the nanofibers developed in this study.

Conclusion

In this work, uniform and homogenous CS/SNP nanofibers with up to 30 w% SN were successfully fabricated via electrospinning under optimized conditions. The average fibre diameter was 149.8 ± 60.76 nm which was not greatly affected by SNP content. FTIR analysis confirmed the incorporation of SNP into the nanofibers. *In* vitro drug release studies revealed that CS/SNP nanofibers were capable of sustainably releasing 37 μg SNP/mg for up to 7 days. Electrospun fibres were rapidly swelled in aqueous environments, necessitating crosslinking. Photo-crosslinking of CS/SNP nanofibers was optimized at 5% TTEGDA concentration and 120W UV irradiation. At these conditions, CS/SNP nanofiber stability and biocompatibility were significantly improved.

CS/SNP nanofibers were more biocompatible to osteoblasts than SNP-free nanofibers. Blending of SNP improved osteoblast viability and reduced cytotoxicity compared to free SNP. The cell viability increased with the SNP content of CS/SNP nanofibers. Fluorescence microscope images revealed that CS/SNP nanofibers improved cell attachment, spreading and proliferation. CS/SNP nanofiber also significantly promoted osteogenic differentiation, as evidenced by elevated expressions of ALP and calcium deposition. The osteogenic differentiation was positively regulated by Smad and Runx2 pathway, which was activated by the crosstalk between SNP and CS nanofibers.

References

[1] Johnell O, Kanis JA. An estimate of the worldwide prevalence and disability associated with osteoporotic fractures. Osteoporosis Int. 2006 Dec;17(12):1726–33. doi: 10.1007/s00198-006-0172-4

[2] Shaw CK, Li YM, Wang LY, et al. Prediction of bone fracture by bone mineral density in Taiwanese. J Formos Med Assoc. 2001;100(12):805–810. PMID: 11802519.

[3] Porter JR, Ruckh TT, Popat KC. Bone tissue engineering: a review in bone biomimetics and drug delivery strategies. Biotechnol Prog. 2009;25(6):1539–1560. doi: 10.1002/btpr.246

[4] Lienemann PS, Lutolf MP, Ehrbar M. Biomimetic hydrogels for controlled biomolecule delivery to augment bone regeneration. Adv Drug Deliv Rev. 2012;64 (12):1078–1089. doi: 10.1016/j.addr.2012.03.010

[5] Yilgor P, Tuzlakoglu K, Reis RL, et al. Incorporation of a sequential BMP-2/BMP-7 delivery system into chitosan-based scaffolds for bone tissue engineering. Biomaterials. 2009;30(21):3551–3559. doi: 10.1016/j.biomaterials.2009.03.024

[6] Srouji S, Ben-David D, Lotan R, et al. Slow-release human recombinant bone morphogenetic protein-2 embedded within electrospun scaffolds for regeneration of bone defect: in vitro and in vivo evaluation. Tissue Eng Part A. 2010;17(3–4):269–277. doi: 10.1089/ten.tea.2010.0250

[7] Kang J, Tada S, Kitajima T, et al. Immobilization of bone morphogenetic protein on DOPA- or dopamine-treated titanium surfaces to enhance osseointegration. Biomed Res Int. 2013;2013:265980. doi: 10.1155/2013/265980

[8] Yun Y-P, Kim SE, Kang EY, et al. The effect of bone morphogenic protein-2 (BMP-2)-immobilizing heparinized-chitosan scaffolds for enhanced osteoblast activity. Tissue Eng Regen Med. 2013;10 (3):122–130. doi: 10.1007/s13770-013-0386-4

[9] Fan J, Park H, Lee MK, et al. Adipose-derived stem cells and BMP-2 delivery in chitosan-based 3D constructs to enhance bone regeneration in a rat mandibular defect model. Tissue Eng Part A. 2014;20(15–16):2169–2179. doi: 10.1089/ten.tea.2013.0523

[10] Tejeda-Montes E, Smith KH, Rebollo E, et al. Bioactive membranes for bone regeneration applications: effect of physical and biomolecular signals on mesenchymal stem cell behavior. Acta Biomaterialia. 2014;10(1):134–141. doi: 10.1016/j.actbio.2013.09.001

[11] Li CH, Wang JW, Ho MH, et al. Immobilization of naringin onto chitosan substrates by using ozone activation. Colloids Surf B Biointerfaces. 2014;115:1–7. doi: 10.1016/j.colsurfb.2013.11.006

[12] Li L, Zhou G, Wang Y, et al. Controlled dual delivery of BMP-2 and dexamethasone by nanoparticle-embedded electrospun nanofibers for the efficient repair of critical-sized rat calvarial defect. Biomaterials. 2015;37:218–229. doi: 10.1016/j.biomaterials.2014.10.015

[13] Evans DM, Ralston SH. Nitric oxide and bone. J Bone Mineral Res. 1996;11(3):300–305. doi: 10.1002/jbmr.5650110303

[14] Saura M, Tarin C, Zaragoza C. Recent insights into the implication of nitric oxide in osteoblast differentiation and proliferation during bone development. ScientificWorldjournal. 2010;10:624–632. doi: 10.1100/tsw.2010.58

[15] Wimalawansa SJ. Nitric oxide: novel therapy for osteoporosis. Expert Opin Pharmacother. 2008;9 (17):3025–3044. doi: 10.1517/14656560802197162

[16] Diwan AD, Wang MX, Jang D, et al. Nitric oxide modulates fracture healing. J Bone Mineral Res. 2000;15(2):342–351. doi: 10.1359/jbmr.2000.15.2.342

[17] Park J-W, Means G. Reaction of drugs with sodium nitroprusside as a source of nitrosamines. Arch Pharm Res. 1991;14(2):118–123. doi: 10.1007/BF02892015

[18] Leeuwenkamp OR, van Bennekom WP, van der Mark EJ, et al. Nitroprusside, antihypertensive drug and analytical reagent. Review of (photo)stability, pharmacology and analytical properties. Pharm Weekbl Sci. 1984;6(4):129–140. doi: 10.1007/BF01954040

[19] Taylor TH, Styles M, Lamming AJ. Sodium nitroprusside as a hypotensive agent in general anaesthesia. Br J Anaesth. 1970;42(10):859–864. doi: 10.1093/bja/42.10.859

[20] Rőszer T. Nitric oxide signaling and nitrosative stress in the musculoskeletal system. In: Laher I, editor Systems biology of free radicals and antioxidants. Berlin Heidelberg: Springer; 2014. pp. 2895–2926.

[21] Felka T, Ulrich C, Rolauffs B, et al. Nitric oxide activates signaling by c-raf, MEK, p-JNK, p38 MAPK and p53 in human mesenchymal stromal cells inhibits their osteogenic differentiation by blocking expression of Runx2. J Stem Cell Res Ther. 2014;4 (04):e1187. doi: 10.4172/2157-7633.1000195

[22] Aitken D, West D, Smith F, et al. Cyanide toxicity following nitroprusside induced hypotension. Can Anaesth Soc J. 1977;24(6):651–660. doi: 10.1007/BF03006709

[23] Lu Y, Slomberg DL, Schoenfisch MH. Nitric oxide-releasing chitosan oligosaccharides as antibacterial agents. Biomaterials. 2014;35(5):1716–1724. doi: 10.1016/j.biomaterials.2013.11.015

[24] Lu Y, Slomberg DL, Shah A, et al. Nitric oxide-releasing amphiphilic poly(amidoamine) (PAMAM) dendrimers as antibacterial agents. Biomacromolecules. 2013;14(10):3589–3598. doi: 10.1021/bm400961r

[25] Nablo BJ, Prichard HL, Butler RD, et al. Inhibition of implant-associated infections via nitric oxide release. Biomaterials. 2005;26(34):6984–6990. doi: 10.1016/j.biomaterials.2005.05.017

[26] Worley BV, Slomberg DL, Schoenfisch MH. Nitric oxide-releasing quaternary ammonium-modified poly(amidoamine) dendrimers as dual action antibacterial agents. Bioconjugate Chem. 2014;25 (5):918–927. doi: 10.1021/bc5000719

[27] Yeom YE, Kim MA, Kim J, et al. Anti-inflammatory effects of the extract of solanum nigrum L. on an acute ear edema mouse model. Mater Technol. 2019;34(14):851–857. doi: 10.1080/10667857.2019.1638671

[28] Thierry B, Merhi Y, Silver J, et al. Biodegradable membrane-covered stent from chitosan-based polymers. J Biomed Mater Res Part A. 2005;75A (3):556–566. doi: 10.1002/jbm.a.30450

[29] Lowe A, Deng W, Smith DW, et al. Coated melt-spun acrylonitrile-based suture for delayed release of nitric oxide. Mater Lett. 2014;125:221–223. doi: 10.1016/j.matlet.2014.03.174

[30] Koh A, Carpenter AW, Slomberg DL, et al. Nitric oxide-releasing silica nanoparticle-doped polyurethane electrospun fibers. ACS Appl Mater Inter. 2013;5(16):7956–7964. doi: 10.1021/am402044s

[31] Koh A, Lu Y, Schoenfisch MH. Fabrication of nitric oxide-releasing porous polyurethane membranes-coated needle-type implantable glucose biosensors. Anal Chem. 2013;85(21):10488–10494. doi: 10.1021/ac402312b

[32] Liu HA, Balkus KJ. Novel delivery system for the bioregulatory agent nitric oxide. Chem Mater. 2009;21(21):5032–5041. doi: 10.1021/cm901358z

[33] Baldik Y, Diwan AD, Appleyard RC, et al. Deletion of iNOS gene impairs mouse fracture healing. Bone. 2005;37(1):32–36. doi: 10.1016/j.bone.2004.10.002

[34] Akins R, Rabolt J. Electrospinning fundamentals and applications. In: Buddy D, RatnerAllan S, HoffmanFrederick J, SchoenJack E, editors. Biomaterials science. 3rd ed. Cambridge, MA, USA: Academic Press; 2013. p. 332–339.

[35] Aadil KR, Nathani A, Sharma CS, et al. Fabrication of biocompatible alginate-poly(vinyl alcohol) nanofibers scaffolds for tissue engineering applications. Mater Technol. 2018;33(8):507–512. doi: 10.1080/10667857.2018.1473234

[36] Chung TW, Lu Y-F, Wang H-Y, et al. Growth of human endothelial cells on different concentrations of gly-arg-gly-asp grafted chitosan surface. Artif Organs. 2003;27(2):155–161. doi: 10.1046/j.1525-1594.2003.07045.x

[37] Sadati SMM, Shahgholian-Ghahfarrokhi N, Shahrousvand E, et al. Edible chitosan/cellulose nanofiber nanocomposite films for potential use as food packaging. Mater Technol. 2021;37(10):1276–1288. doi: 10.1080/10667857.2021.1934367

[38] Lehr CM, Bouwstra JA, Schacht EH, et al. In vitro evaluation of mucoadhesive properties of chitosan and some other natural polymers. Int J Pharmaceut. 1992;78(1–3):43–48. doi: 10.1016/0378-5173(92)90353-4

[39] He P, Davis SS, Illum L. In vitro evaluation of the mucoadhesive properties of chitosan microspheres. Int J Pharmaceut. 1998;166(1):75–88. doi: 10.1016/S0378-5173(98)00027-1

[40] Wang K, Buschle-Diller G, Misra RDK. Chitosan-based injectable hydrogels for biomedical. Mater Technol. 2015;30(sup5):B198–B205. doi: 10.1179/17535557B15Y.000000008

[41] Ho MH, Liao MH, Lin YL, et al. Improving effects of chitosan nanofiber scaffolds on osteoblast proliferation and maturation. Int J Nanomedicine. 2014 Sep 9;9:4293–4304. doi: 10.2147/IJN.S68012

[42] Salehi F, Hossein B, Gholamreza K, et al. Chitosan promotes ROS-mediated apoptosis and S phase cell cycle arrest in triple-negative breast cancer cells: evidence for intercalative interaction with genomic DNA. RSC Adv. 2017;7(68):43141–43150. doi: 10.1039/C7RA06793C

[43] Liu D, Shu G, Jin F, et al. ROS-responsive chitosan-SS31 prodrug for AKI therapy via rapid distribution in the kidney and long-term retention in the renal tubule. Sci Adv. 2020 Oct 9;6(41):eabb7422. doi: 10.1126/sciadv.abb7422

[44] Vesey CJ, Batistoni GA. The determination and stability of sodium nitroprusside in aqueous solutions (determination and stability of SNP). J Clin Pharm Therapeutics. 1977;2(2):105–117. doi: 10.1111/j.1365-2710.1977.tb00080.x

[45] Park ES, Lind A-K, Dahm-Kähler P, et al. RUNX2 transcription factor regulates gene expression in luteinizing granulosa cells of rat ovaries. Mol Endocrinol. 2010;24(4):846–858. doi: 10.1210/me.2009-0392

[46] Cho J, Heuzey M-C, Bégin A, et al. Viscoelastic properties of chitosan solutions: effect of concentration and ionic strength. J Food Eng. 2006;74(4):500–515. doi: 10.1016/j.jfoodeng.2005.01.047

[47] Son WK, Youk JH, Lee TS, et al. Electrospinning of ultrafine cellulose acetate fibers: Studies of a new solvent system and deacetylation of ultrafine cellulose acetate fibers. J Polym Sci B Polym Phys. 2004;42 (1):5–11. doi: 10.1002/polb.10668

[48] Mit-Uppatham C, Nithitanakul M, Supaphol P. Ultrafine electrospun polyamide-6 fibers: effect of solution conditions on morphology and average fiber diameter. Macromole Chem Phys. 2004;205 (17):2327–2338. doi: 10.1002/macp.200400225

[49] Deitzel JM, Kleinmeyer J, Harris D, et al. The effect of processing variables on the morphology of electrospun nanofibers and textiles. Polymer. 2001;42 (1):261–272. doi: 10.1016/S0032-3861(00)00250-0

[50] Demir MM, Yilgor I, Yilgor E, et al. Electrospinning of polyurethane fibers. Polymer. 2002;43 (11):3303–3309. doi: 10.1016/S0032-3861(02)00136-2

[51] Sangsanoh P, Supaphol P. Stability improvement of electrospun chitosan nanofibrous membranes in neutral or weak basic aqueous solutions. Biomacromolecules. 2006;7(10):2710–2714. doi: 10.1021/bm060286l

[52] Holzbecher M, Knop O, Falk M. Infrared studies of water in crystalline hydrates: sodium nitroprusside dihydrate, na2[Fe(cn)5NO]•2H2O Na2[Fe(CN) 5NO]•2H2O. Can J Chem. 1971;49(9):1413–1424. doi: 10.1139/v71-233

[53] Tang S, Edman L. On-demand photochemical stabilization of doping in light-emitting electrochemical cells. Electrochimica Acta. 2011;56(28):10473–10478. doi: 10.1016/j.electacta.2011.01.073

[54] Wold KA, Damodaran VB, Suazo LA, et al. Fabrication of biodegradable polymeric nanofibers with covalently attached NO donors. ACS Appl Mater Inter. 2012;4(6):3022–3030. doi: 10.1021/am300383w

[55] Worley BV, Soto RJ, Kinsley PC, et al. Active release of nitric xxide-releasing dendrimers from electrospun polyurethane fibers. ACS Biomater Sci Eng. 2016;2(3):426–437. doi: 10.1021/acsbiomaterials.6b00032

[56] Bakolitsa C, Cohen DM, Bankston LA, et al. Structural basis for vinculin activation at sites of cell adhesion. Nature. 2004;430(6999):583–586. doi: 10.1038/nature02610

[57] Keselowsky BG, Collard DM, García AJ, Integrin binding specificity regulates biomaterial surface chemistry effects on cell differentiation. Proc Natl Acad Sci; USA. 2005. Apr 26;102(17):5953–7. doi: 10.1073/pnas.0407356102

[58] Haÿ E, Lemonnier L, Modrowski D, et al. N- and E-cadherin mediate early human calvaria osteoblast differentiation promoted by bone morphogenetic protein-2. J Cell Physiol. 2000;Apr 183(1):117–128. doi: 10.1002

[59] Civitelli R. Cell–cell communication in the osteoblast/osteocyte lineage. Arch Biochem Biophys. 2008;473 (2):188–192. doi: 10.1016/j.abb.2008.04.005

[60] Stains JP, Civitelli R. Cell-to-cell interactions in bone. Biochem Biophys Res Commun. 2005;328 (3):721–727. doi: 10.1016/j.bbrc.2004.11.078

[61] Kim SM, Yuen T, Iqbal J, et al. The NO–cGMP–PKG pathway in skeletal remodeling. Ann N Y Acad Sci. 2021;1487(1):21–30. doi: 10.1111/nyas.14486

[62] Lai CF, Chaudhary L, Fausto A, et al. Erk is essential for growth, differentiation, integrin expression, and cell function in human osteoblastic cells. J Biol Chem. 2001;276(17):14443–14450. doi: 10.1074/jbc.M010021200

[63] Rangaswami H, Marathe N, Zhuang S, et al. Type II cGMP-dependent protein kinase mediates osteoblast mechanotransduction. J Biol Chem. 2009;284 (22):14796–14808. doi: 10.1074/jbc.M806486200

[64] Huang RL, Yuan Y, Tu and J, et al. Opposing TNF-α/ IL-1β- and BMP-2-activated MAPK signaling pathways converge on Runx2 to regulate BMP-2-induced osteoblastic differentiation. Cell Death Dis. 2014;5(4): e1187. doi: 10.1038/cddis.2014.101